

Built-In Electric Field in Freestanding Hydroxide/Sulfide Heterostructures for Industrially Relevant Oxygen Evolution

Wentong Wu⁺, Yueshuai Wang⁺, Shizhen Song, Zhichao Ge, Chunyang Zhang, Jie Huang, Guiren Xu, Ning Wang, Yue Lu, Zhanfeng Deng, Haohong Duan, Maochang Liu,* and Cheng Tang*

Abstract: Alkaline water electrolysis (AWE), as a premier technology to massively produce green hydrogen, hinges on outstanding oxygen evolution reaction (OER) electrodes with high activity and robust stability under high current densities. However, it is often challenged by issues such as catalytic layer shedding, ion dissolution, and inefficient bubble desorption. Herein, a scalable corrosion-electrodeposition method is presented to synthesize nickel–iron layered double hydroxide (NiFe-LDH)/Ni₃S₂ heterostructures on nickel mesh, tailored to meet the stringent requirements of industrial AWE. The study underscores the critical role of the built-in electric field (BEF) in optimizing electronic properties, curtailing Fe leaching, and enhancing mass transfer. The resultant NiFe-LDH/Ni₃S₂ heterostructure manifests remarkable OER performance, with ultra-low overpotentials of 202 mV at 10 mA cm⁻² and 290 mV at 800 mA cm⁻² in 1.0 M KOH at 25 °C, alongside superior steady-state stability and resistance to reverse current under fluctuating conditions. Furthermore, the performance is further validated in an alkaline electrolyzer, achieving a large current density of 800 mA cm⁻² at a cell voltage of 1.908 V, while maintaining excellent stability. This work offers a blueprint for the design of efficient OER electrodes for industrially relevant AWE applications.

Introduction

Alkaline water electrolysis (AWE) stands out as a leading technology for green hydrogen production, offering the benefits of technological maturity and cost-effectiveness^[1–4]. Despite these advantages, AWE grapples with challenges such as low operating current densities (250–500 mA cm⁻²) and high energy consumption (exceeding 4.5 kWh Nm⁻³ H₂).^[5] As the direct site for electrocatalytic reaction, the electrode becomes one of the most core components in the AWE system.^[6] Prior studies have underscored the pivotal role of electrode overpotential reduction in enhancing the energy conversion efficiency of water electrolysis.^[7–9]

Although numerous electrocatalysts have demonstrated impressive performance under benign laboratory conditions (e.g., 1.0 M KOH, 25 °C),^[10–13] they often falter under harsh industrial conditions (e.g., 30 wt% KOH, 80–90 °C), where issues such as catalyst layer delamination, swift ion depletion, and bubble accumulation arise.^[14–16] Bridging the gap between laboratory and industrial conditions is thus imperative for advancing our understanding of AWE on an industrial scale.^[17]

Freestanding nickel mesh (NM) and Raney nickel (Raney Ni) dominate current industrial applications for hydrogen evolution reaction (HER) at the cathode and oxygen evolution reaction (OER) at the anode.^[2] Yet, their performance

[*] W. Wu⁺, Z. Ge, C. Zhang, J. Huang, M. Liu
International Research Center for Renewable Energy, State Key Laboratory of Multiphase Flow in Power Engineering, Xi'an Jiaotong University, Xi'an, Shaanxi 710049, P.R. China
E-mail: maochangliu@mail.xjtu.edu.cn

C. Tang
Tsinghua Center for Green Chemical Engineering Electrification, Beijing Key Laboratory of Green Chemical Reaction Engineering and Technology, Department of Chemical Engineering, Tsinghua University, Beijing 100084, P.R. China
E-mail: cheng-net0@tsinghua.edu.cn

W. Wu⁺, Y. Wang⁺, S. Song, Z. Ge, G. Xu, N. Wang, Y. Lu, Z. Deng, C. Tang
Beijing Institute of Smart Energy, Beijing 102209, P.R. China

S. Song
State Key Laboratory of Electrical Insulation and Power Equipment, Xi'an Jiaotong University, Xi'an, Shaanxi 710049, P.R. China

G. Xu
Institute for Advanced Materials and Technology, University of Science and Technology Beijing, Beijing 100083, P.R. China

Y. Wang⁺, Y. Lu
State Key Laboratory of Materials Low-Carbon Recycling, College of Materials Science and Engineering, Beijing University of Technology, Beijing 100124, P.R. China

H. Duan
Department of Chemistry, Tsinghua University, Beijing 100084, P.R. China

C. Tang
Ordos Laboratory, Inner Mongolia 017000, P.R. China

[+] Both authors contributed equally to this work.

Additional supporting information can be found online in the Supporting Information section

is difficult to fulfill the ambitious targets (U.S. Department of Energy: 1.0 A cm^{-2} @ 1.80 V per cell and lifetime of 80 000 h, 2026, and European Commission: 1.0 A cm^{-2} @ 1.80 V per cell, 2030).^[5] Compared with HER, OER involves four proton-coupled electron transfer reactions and becomes the rate-determining step (RDS) of the water electrolysis process, making the development of efficient OER catalysts essential for curtailing overall energy consumption in hydrogen production.^[18] A qualified industrial alkaline OER electrode should have at least four metrics: 1) low cost and scalable production; 2) excellent catalytic activity and stability, especially at high current density ($\geq 500 \text{ mA cm}^{-2}$), which is crucial for the economy viability of electrolyzers^[18,19]; 3) superior mass transfer capabilities.^[20] Operation conditions with high current densities involve rapid electrolyte depletion and gas evolution, thus the good affinity of electrode surface to OH^- is of great significance for accelerating the kinetics of electrode interface reaction.^[21,22] 4) resistance to fluctuating conditions,^[23] which usually accelerates the failure of catalytic layers in industrial electrolyzers.^[24] Consequently, the quest for integrated OER electrodes that can operate with high current densities and maintain robust stability under industrial conditions remains the cornerstone of the AWE system.

Considering the aforementioned criteria, transition metal hydroxides, especially nickel-iron layered double hydroxide (NiFe-LDH), have been well demonstrated as favorable OER electrocatalysts.^[25–27] It is due to the high intrinsic activity, large specific surface area,^[28] cost-effectiveness, and tunability.^[29] However, the intrinsic limitations, such as low conductivity and powdery form, make it liable to fall off and fail, especially under high current densities.^[30,31] More critically, its thermodynamic instability results in the overoxidation of Fe (such as FeO_4^{2-}) and thus significant leaching,^[32,33] particularly under high temperatures and potentials.^[34] Addressing these challenges through NiFe-LDH modification and adaptation to industrial conditions is thus imperative. Studies have indicated that the built-in electric field (BEF), generated by integrating components with disparate Fermi levels, is an effective approach to optimizing the electronic structure and surface properties of catalysts.^[35–38]

In this work, we designed a freestanding NiFe-LDH/ Ni_3S_2 heterostructure supported on NM substrates for industrially relevant AWE applications. The distinct work functions of NiFe-LDH and Ni_3S_2 facilitate charge transfer across the heterointerface, establishing a robust BEF. By comprehensive characterizations and theoretical study, we revealed the role of BEF in enhancing OH^- adsorption and mitigating Fe leaching. Consequently, the developed electrode demonstrated superior electrochemical performance, achieving remarkably low overpotentials of 202 mV at 10 mA cm^{-2} and 290 mV at 800 mA cm^{-2} in 1.0 M KOH at 25°C , coupled with outstanding steady-state stability and resilience to operational fluctuations. Furthermore, the performance in AWE electrolyzers has been validated, requiring only 1.908 V for a large current density of 800 mA cm^{-2} and exhibiting commendable stability.

Results and Discussion

As illustrated in Figure 1a, the NiFe-LDH/ Ni_3S_2 heterostructure was synthesized through a scalable corrosion-electrodeposition process. Initially, a rough Ni_3S_2 transition layer was in situ grown on the surface of NM by room temperature vulcanization (denoted as Ni_3S_2). Subsequently, NiFe-LDH nanosheets were electrodeposited on the surface of Ni_3S_2 (denoted as NiFe-LDH/ Ni_3S_2). Notably, the local magnification indicates an ordered hierarchy between NM, Ni_3S_2 , and NiFe-LDH. Scanning electron microscopy (SEM) image shows that the pristine NM displays a smooth surface, less optimal for the even deposition of active NiFe-LDH nanosheets (Figure 1b, Figure S1). The in situ growth of Ni_3S_2 on the NM surface enhances the surface roughness (Figure 1c), thereby providing an enhanced adhesion strength for the deposition of NiFe-LDH. SEM image and elemental mapping confirm the uniform distribution of NiFe-LDH on the Ni_3S_2 layer (Figure 1d,e). Cross-sectional SEM analysis (Figure 1f, Figure S2) discloses a $\approx 200\text{-nm}$ Ni_3S_2 layer atop the NM, capped by a $\approx 300\text{-nm}$ NiFe-LDH layer. Furthermore, transmission electron microscopy (TEM) images and elemental mapping elucidate the intimate interfacial coupling between Ni_3S_2 and NiFe-LDH (Figure 1g). The high-resolution TEM (HRTEM) image (Figure 1h, Figure S3) with distinct lattice fringes further reveals the strongly coupled heterointerface between Ni_3S_2 and NiFe-LDH.

The construction of BEF between Ni_3S_2 and NiFe-LDH was verified by ultraviolet photoelectron spectroscopy (UPS), X-ray photoelectron spectroscopy (XPS), and UV/Vis diffuse reflection spectra (DRS). The electron transfer behavior within semiconductor heterostructures is inherently linked to the work function difference ($\Delta\Phi$), which drives the electron transfer between the interface until the Fermi level equilibrium.^[39,40] UPS was utilized to obtain work functions (Φ) values of Ni_3S_2 and NiFe-LDH (Figure 2a). The calculated Φ values are 3.01 eV for Ni_3S_2 and 2.48 eV for NiFe-LDH, indicating a substantial $\Delta\Phi$ of 0.53 eV across the interface. This result indicates that during the formation of the interface between Ni_3S_2 and NiFe-LDH, NiFe-LDH spontaneously transfers electrons to Ni_3S_2 ,^[41] which is further supported by XPS analysis. NiFe-LDH/ Ni_3S_2 shows upward shifts of 0.5 and 0.4 eV of the binding energy in the Ni 2p and Fe 2p region compared with those of NiFe-LDH, respectively (Figure 2b,c), verifying spontaneous electron transfer from NiFe-LDH to Ni_3S_2 under the driving force of $\Delta\Phi$ to equilibrium Fermi level.^[35] In addition, UV/Vis DRS shows that the heterostructure possesses a narrower bandgap than that of Ni_3S_2 , an effect attributed to the incorporation between the Ni_3S_2 transition layer and NiFe-LDH (Figure 2d, Figure S4). Therefore, the energy band diagram based on UPS and UV/Vis DRS shows the energy level relationship in detail (Figure S5). The result demonstrates that the large $\Delta\Phi$ offers the desirable driving force for electron flow from high level to low level and spontaneously creates a robust interfacial BEF with the direction pointing from NiFe-LDH to Ni_3S_2 (Figure 2e). The interfacial BEF with unidirectional electron transfer most likely via Fe–S and Ni–S bonding

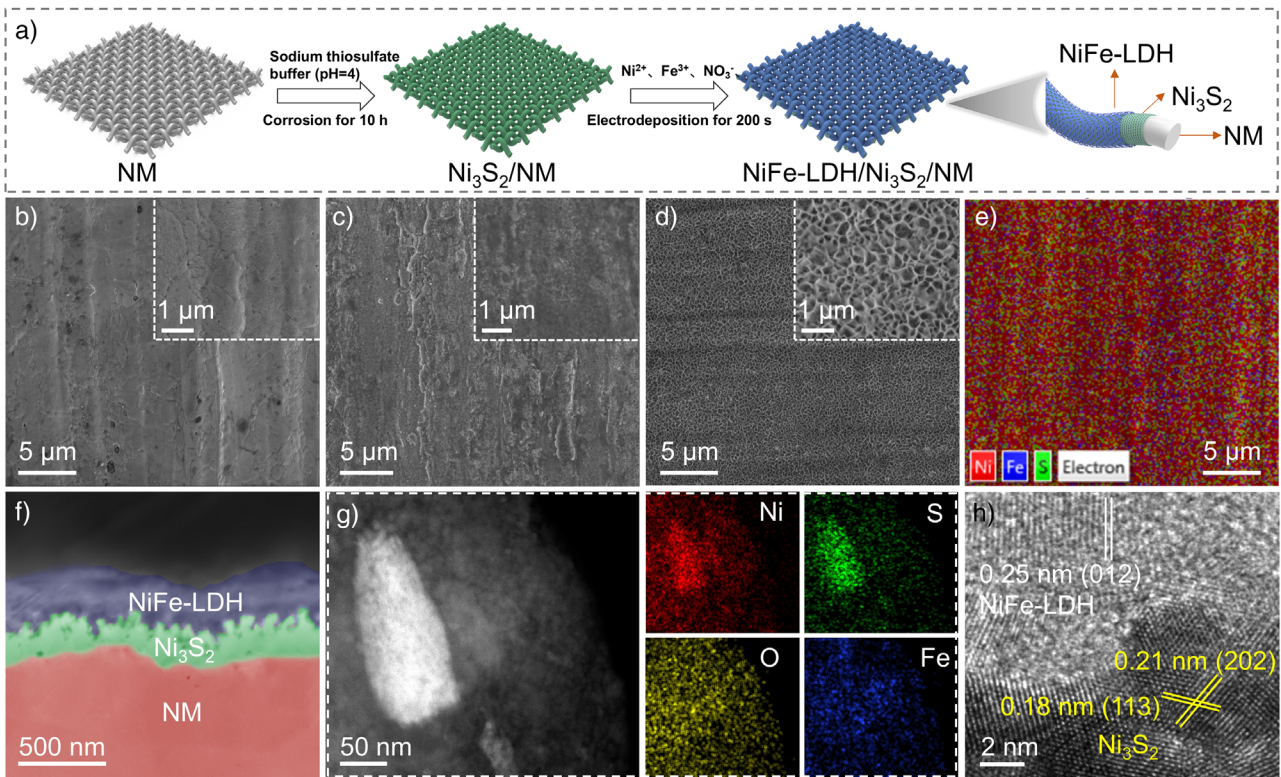


Figure 1. The fabrication and structural characterization of NiFe-LDH/Ni₃S₂ heterostructure. a) Schematic of the synthesis of NiFe-LDH/Ni₃S₂ electrode. b-d) SEM images of cleaned NM, Ni₃S₂, and NiFe-LDH/Ni₃S₂ electrodes, respectively. e) Elemental mapping of NiFe-LDH/Ni₃S₂ electrode. f) Cross-sectional SEM image of NiFe-LDH/Ni₃S₂. g) HRTEM image and EDS mapping of NiFe-LDH/Ni₃S₂. h) HRTEM image of NiFe-LDH/Ni₃S₂, showing the interface.

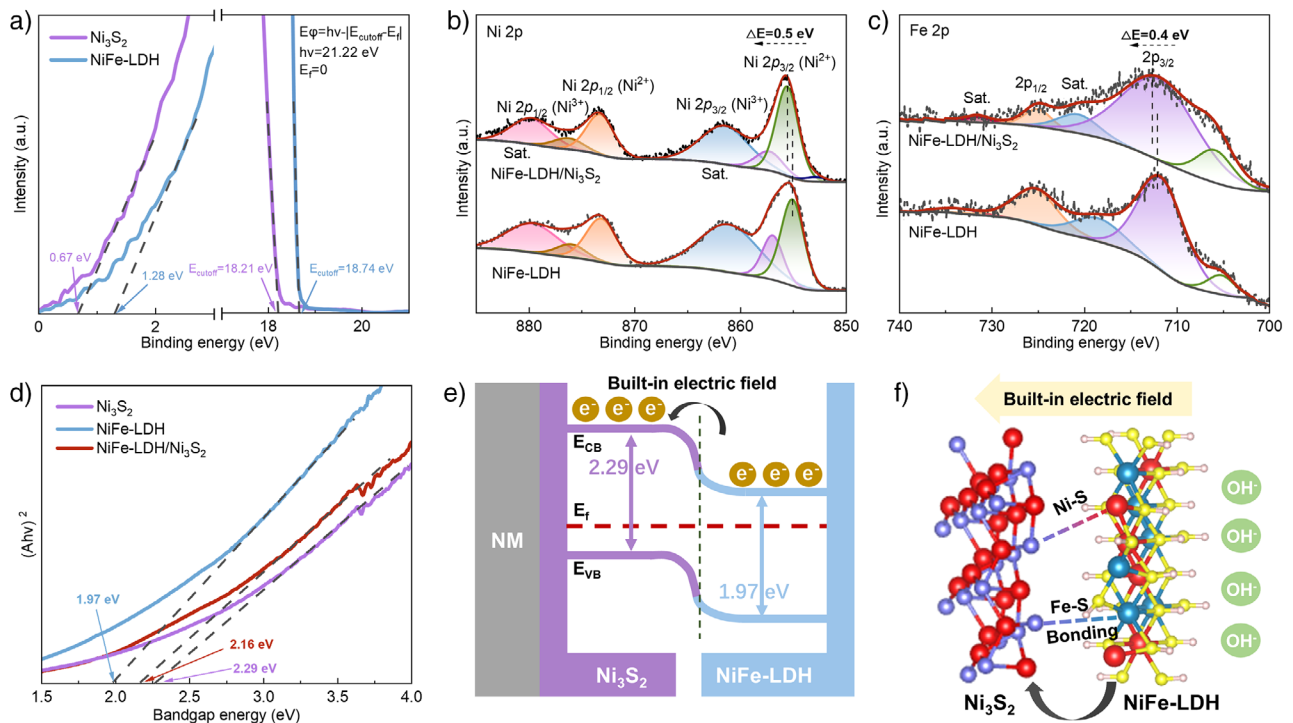


Figure 2. Compositional characterizations and analysis of NiFe-LDH/Ni₃S₂ heterostructure. a) UPS spectra of Ni₃S₂ and NiFe-LDH. b) High-resolution XPS spectra for Ni 2p and c) Fe 2p. d) UV/Vis DRS spectra of Ni₃S₂, NiFe-LDH, and NiFe-LDH/Ni₃S₂. e) Energy band diagram of Ni₃S₂ and NiFe-LDH in the heterostructure. f) The interface structure diagram between Ni₃S₂ and NiFe-LDH.

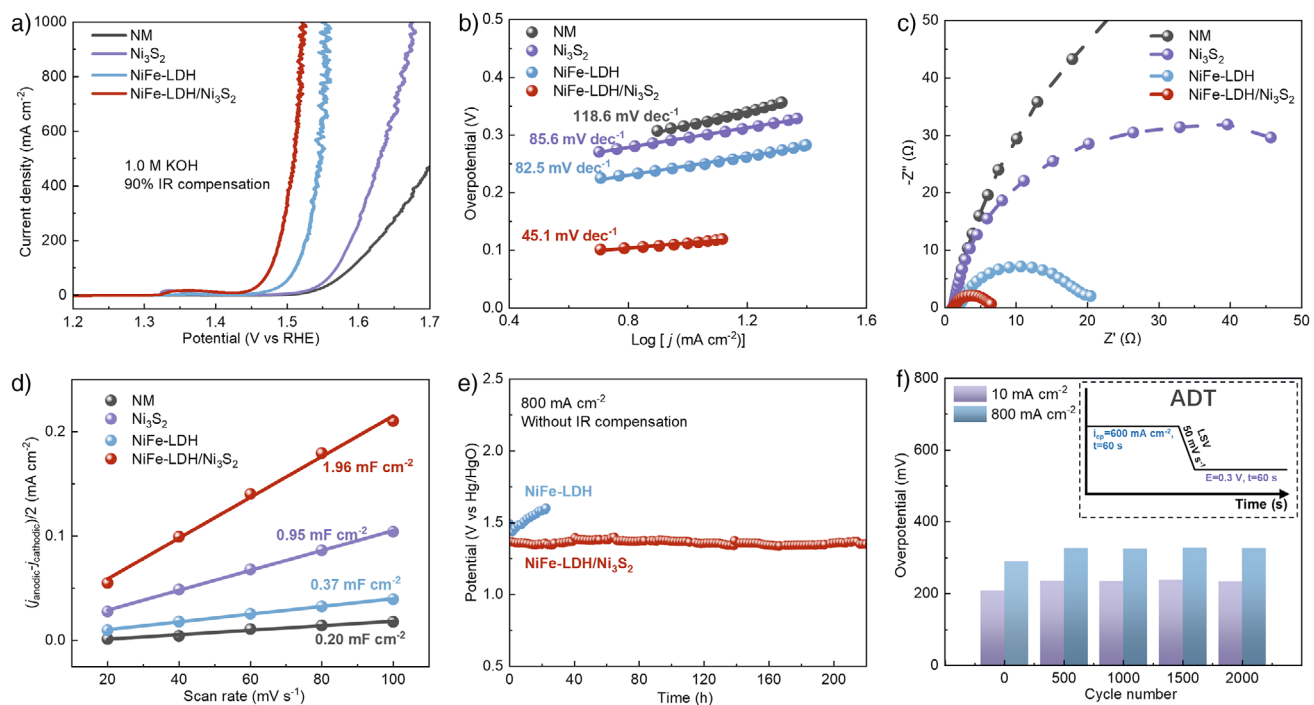


Figure 3. Electrochemical measurements of NiFe-LDH/Ni₃S₂ in 1.0 M KOH. a) Polarization curves, b) Tafel plots, c) EIS Nyquist plots, and d) C_{dl} of cleaned NM, Ni₃S₂, NiFe-LDH, and NiFe-LDH/Ni₃S₂ electrodes, respectively. e) Chronopotentiometry test of NiFe-LDH and NiFe-LDH/Ni₃S₂ at 800 mA cm⁻². f) ADT tests of NiFe-LDH/Ni₃S₂.

can effectively modulate the charge separation (Figure 2f), which simultaneously induces the electron-rich Ni₃S₂ region and electron-deficient NiFe-LDH region, thus enhancing the surface adsorption of OH⁻.^[41]

To evaluate the OER activity, the polarization curves for the NiFe-LDH/Ni₃S₂ heterostructure, together with those for NiFe-LDH, Ni₃S₂, and pristine NM, are presented in Figure 3a and Figure S6. Specifically, the heterostructure demonstrates an ultralow overpotential, requiring merely 202 mV to reach a current density of 10 mA cm⁻², significantly outperforming NiFe-LDH (234 mV), Ni₃S₂ (288 mV), and NM (313 mV). The OER kinetics were further elucidated through the Tafel slope, and a smaller slope is indicative of more favorable reaction kinetics.^[42] The NiFe-LDH/Ni₃S₂ heterostructure exhibits a low Tafel slope of 45.1 mV dec⁻¹, substantially lower than that of NiFe-LDH (82.6 mV dec⁻¹), Ni₃S₂ (85.6 mV dec⁻¹), and NM (118.6 mV dec⁻¹), underscoring its superior reaction kinetics for OER process (Figure 3b). Electrochemical impedance spectroscopy (EIS) was utilized to probe the charge-transfer kinetics of electrocatalysts. The NiFe-LDH/Ni₃S₂ heterostructure displays the smallest charge-transfer resistance (R_{ct}) in the EIS Nyquist plots, indicative of the fastest charge transfer among all samples (Figure 3c). Notably, in the case of the same solution resistance, the incorporation of the Ni₃S₂ transition layer into the heterostructure yields a marked reduction in ohmic resistance (R_{ohm}) compared to NiFe-LDH (Figure S7), further verifying that the introduction of the transition layer increased the connection strength between the catalytic layer and the NM. The electrochemically active surface area (ECSA), which is proportional to the electrochemical double-layer capacitance

(C_{dl}), is a critical parameter for evaluating electrocatalytic activity.^[43] Meanwhile, the C_{dl} values can also be used to quantify surface area (Figure 3d, Figure S8). The C_{dl} value of NiFe-LDH/Ni₃S₂ is calculated to be 1.96 mF cm⁻², noticeably larger than those of NiFe-LDH, Ni₃S₂, and NM. The presence of a heterointerface can provide more accessible active sites for improved OER performance. Furthermore, the wettability of electrodes was investigated by contact angle tests (Figure S9). The NiFe-LDH/Ni₃S₂ heterostructure exhibits significantly improved hydrophilicity and aerophobicity, suggesting that the electrolyte can be replenished in time to resist rapid depletion under high current densities. The smaller Tafel slope, R_{ct} , R_{ohm} , larger ECSA, and improved hydrophilicity illustrate the enhanced intrinsic activity and enriched active sites contributed by the formation of interfacial BEF, further underpinning the remarkable OER activities.

In addition to improving the electrode activity, the BEF construction has a significant influence on the stability of NiFe-LDH. The steady long-term stability was first evaluated by chronopotentiometry (CP) tests. NiFe-LDH/Ni₃S₂ shows a negligible degradation in OER activity over an extended period exceeding 200 h at a high current density of 800 mA cm⁻², in stark contrast to the rapidly deteriorating performance of NiFe-LDH (Figure 3e, Figure S10). Polarization curves and SEM images after stability show that the performance is almost not attenuated, and the morphology is slightly agglutinated due to surface reconstruction (Figures S11 and S12). Cross-sectional SEM images show that the hierarchical heterogeneous structure remains stable (Figure S13). Most importantly, TEM images and corresponding energy dispersive spectroscopy (EDS) mapping reveal that

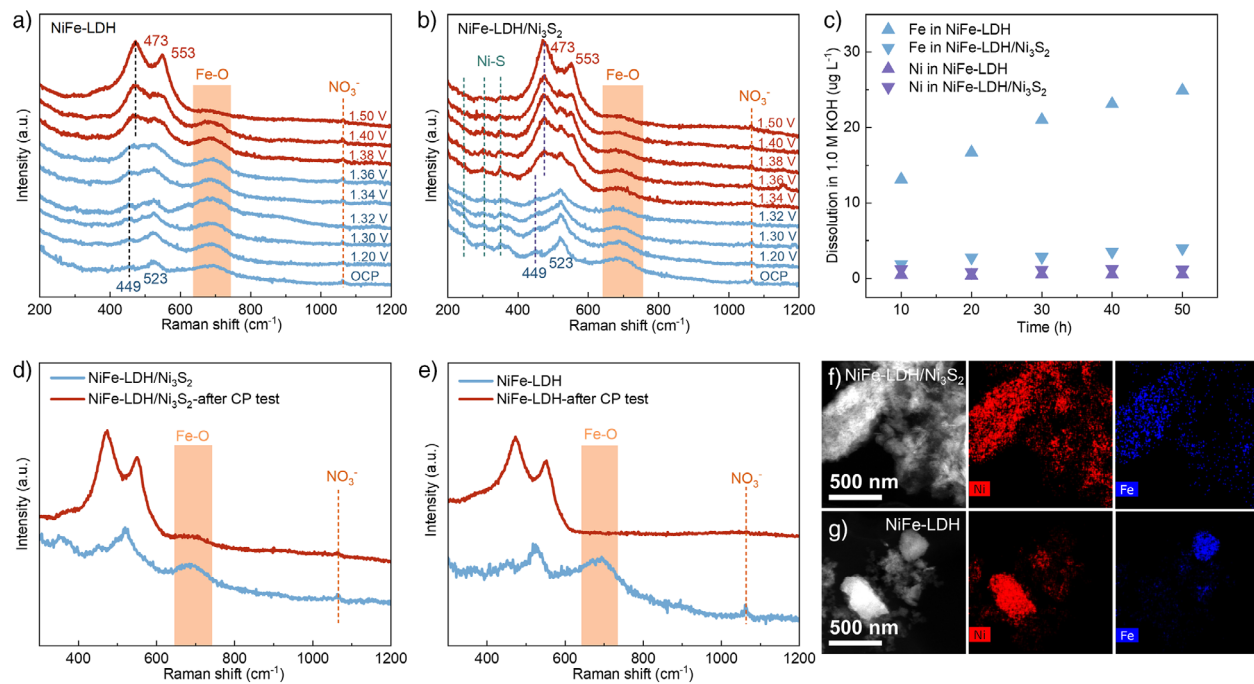


Figure 4. Mechanism analysis of performance improvement between NiFe-LDH and NiFe-LDH/Ni₃S₂. a) In situ Raman spectra of NiFe-LDH and b) NiFe-LDH/Ni₃S₂ under different potentials vs RHE. c) The dissolution of Ni and Fe species from NiFe-LDH and NiFe-LDH/Ni₃S₂ obtained by ICP-MS during the CP tests. d) Raman spectra of NiFe-LDH/Ni₃S₂ and e) NiFe-LDH before and after CP tests. f) TEM image and EDS mapping of NiFe-LDH/Ni₃S₂ after CP tests. g) TEM image and EDS mapping of NiFe-LDH after CP tests.

the oxidation state of S increases, and the transition layer transforms from S²⁻ to SO_x²⁻. The results confirm the electron transfer from S to Fe, as the transition layer did not directly participate in the surface electrode reaction (Figure S14). In addition, accelerated durability tests (ADT) were conducted to evaluate the resistance to reverse current during start-stop operations for AWEs powered by fluctuating renewable energy.^[44] The inset in Figure 3f illustrates a single cycle of the ADT process (a constant current process of 600 mA cm⁻² for 60 s, a linear sweep voltammetry, and a constant potential process of 0.3 V vs RHE for 60 s). After 2000 cycles, the catalyst exhibits only a modest increase in overpotential by 30 and 34 mV at 10 and 800 mA cm⁻² after the initial 500 cycles, indicating a slight attenuation in the early stage followed by a stable performance in the subsequent cycles (Figure 3f, Figure S15).

The reaction mechanism and electrocatalyst reconstruction were investigated by in situ Raman measurements (Figure 4a,b). The presence of interlayer anion intercalation, indicated by the NO₃⁻ signal, affirms the identity of NiFe-LDH.^[45] A distinct Fe–O signal is observed at the open circuit potential (OCP). Compared with NiFe-LDH/Ni₃S₂, the Fe–O signal in NiFe-LDH is significantly reduced at high potential due to overoxidation and Fe leaching.^[41] Concurrently, the Ni–O vibrational peaks exhibit noticeable shifts, with the hydroxide bands at 449 and 523 cm⁻¹ transitioning to 473 and 553 cm⁻¹, corresponding to the bending and stretching modes of N^{III}–O in γ-NiOOH, respectively.^[46,47] The NiFe-LDH/Ni₃S₂ demonstrates pronounced spectral changes at lower potentials, suggesting an accelerated phase transition that correlates with its enhanced OER performance.^[48] The

chemical stability of the heterostructure was interrogated using inductively coupled plasma-mass spectrometry (ICP-MS), Raman spectroscopy, and TEM. Concretely, ICP-MS monitored the amount of Fe dissolution in the alkaline environment (1.0 M KOH) under a high current density (800 mA cm⁻²). The results show that NiFe-LDH exhibits rapid Fe leaching, and by the introduction of BEF, a slow Fe leaching is displayed in NiFe-LDH/Ni₃S₂ (Figure 4c). Raman spectroscopy before and after CP tests reveals that while both NiFe-LDH/Ni₃S₂ and NiFe-LDH undergo NiOOH reconstruction, the former retains a discernible Fe–O peak and NO₃⁻ signal (Figure 4d). In contrast, the latter shows diminished Fe–O and NO₃⁻ signals, indicative of significant Fe loss and altered structure (Figure 4e). Combined with the results in Figure 4a, it is shown that the long-term OER reaction at high potential leads to continuous Fe leaching. TEM images after the CP test confirm an even distribution of Ni and Fe in the heterostructure (Figure 4f), in stark contrast to the phase segregation observed in NiFe-LDH, a result of Fe ion re-deposition following significant loss (Figure 4g, Figure S16). The deactivation of NiFe-LDH at high current densities is attributed to the formation of less active Fe(OH)₃ during Fe ion re-deposition.^[15] The introduction of the Ni₃S₂ transition layer constructs a BEF with NiFe-LDH, where the negatively charged S in the interface Fe–S bonding serves as an electron reservoir.^[41] During the OER process, electrons are potentially transferred from S to Fe, thereby effectively preventing overoxidation and loss of Fe and enhancing the stability of NiFe-LDH.

The function mechanism of interfacial bonding and BEF on the stability and activity was further studied by density

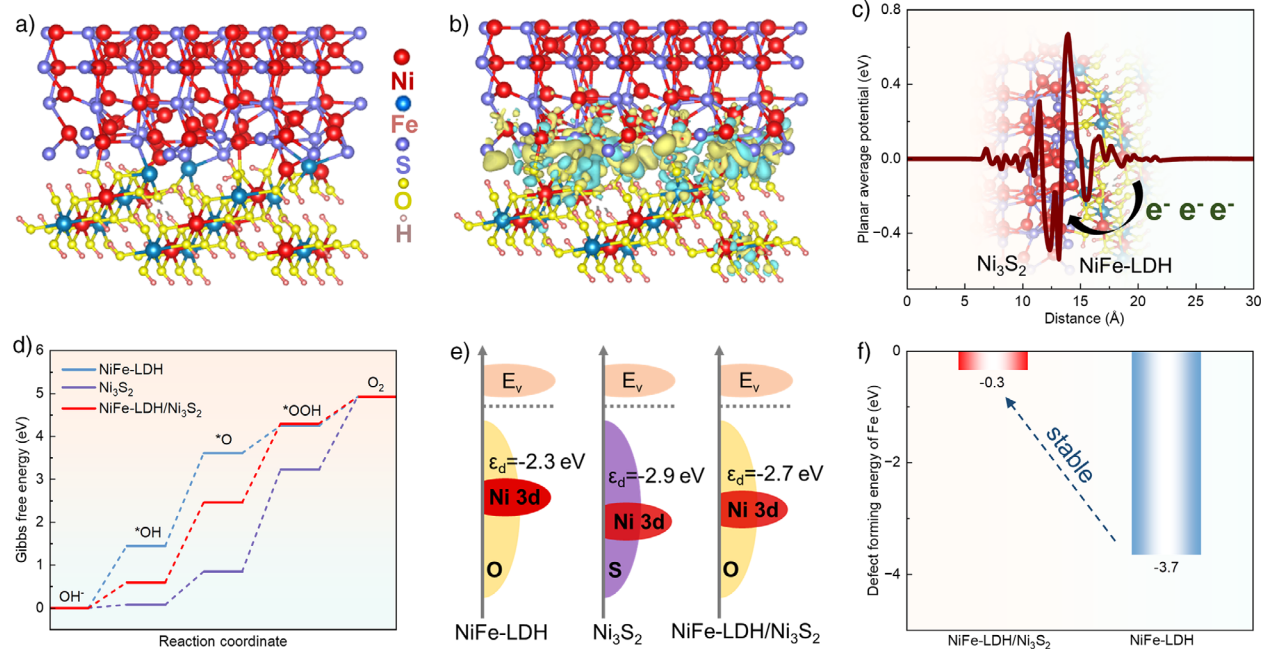


Figure 5. Theoretical calculations on activity and stability enhancement. a) The optimized theoretical model of NiFe-LDH/Ni₃S₂. b) Charge density difference of NiFe-LDH/Ni₃S₂. c) Planer average potential diagram of the interface between NiFe-LDH and Ni₃S₂. d) Adsorption-free energy of oxygen intermediates on Ni₃S₂, NiFe-LDH, and NiFe-LDH/Ni₃S₂. e) Schematic of d-band center of Ni₃S₂, NiFe-LDH, and NiFe-LDH/Ni₃S₂, respectively. f) Defect forming energy of Fe for NiFe-LDH and NiFe-LDH/Ni₃S₂, respectively.

functional theory (DFT) calculations. We selected the (012) facet of NiFe-LDH and the (202) facet of Ni₃S₂ to model the interface (Figure 5a, Figure S17), aligning with experimental data. The charge density difference quantitatively exposes electron transfer behavior, with yellow and cyan regions indicating electron accumulation and depletion, respectively (Figure 5b).^[41] This asymmetrical electron distribution at the interface substantiates the establishment of a BEF between NiFe-LDH and Ni₃S₂. The plane average potential diagram more distinctly shows the electron dissipation from NiFe-LDH and the accumulation in Ni₃S₂ (Figure 5c), consistent with XPS and UPS results. In addition, the adsorption-free energy of oxygen intermediates was calculated to explore the relationship between the reaction pathway and OER performance. The four steps of the OER process on the optimized models, including *OH, *O, and *OOH intermediates, are detailed in Figure 5d. For NiFe-LDH, the RDS involves the deprotonation of *OH to *O, with a barrier of 2.16 eV. Notably, the NiFe-LDH/Ni₃S₂ lowers this barrier to 1.86 eV, indicating a thermodynamic advantage for the OER process. The density of state (DOS) results show that the NiFe-LDH/Ni₃S₂ possesses a higher carrier density near the Fermi level (Figure S18), indicating its faster electron transfer capability.^[49] Understanding the correlation between electronic structure change and d-band center (ϵ_d) is of great significance for exploring the underlying catalytic mechanism.^[50] As shown in Figure 5e, the ϵ_d of NiFe-LDH and Ni₃S₂ are -2.3 and -2.9 eV, respectively. In comparison, the NiFe-LDH/Ni₃S₂ heterostructure presents a moderate ϵ_d of -2.7 eV, potentially optimizing oxygen intermediate adsorption and boosting electrocatalytic activity. Furthermore, the construction of BEF is beneficial to resist

the overoxidation and ion loss of Fe during the OER process. As shown in Figure 5f, the defect formation energy of Fe could be a decisive factor in the stability at high current densities.^[11] Compared with pristine NiFe-LDH, the defect formation energy of Fe in NiFe-LDH/Ni₃S₂ heterostructure substantially decreases from -3.7 to -0.3 eV, indicating greatly improved antioxidation properties. Owing to the formation of Fe–S bonds at the heterostructure interface (Figure 5a), the electron-rich S sites tend to donate electrons to Fe, thereby significantly mitigating overoxidation and leaching during OER under the action of the BEF.

To assess the practical feasibility of developed electrodes, electrocatalytic performance was further evaluated under industrially relevant conditions, e.g., 80 °C in 30 wt % KOH solution (Figure 6a). Within a three-electrode configuration, the NiFe-LDH/Ni₃S₂ heterostructure electrode displays superior activity, requiring an overpotential of merely 235 mV to achieve 800 mA cm⁻², much lower than 262 mV for NiFe-LDH, 288 mV for Ni₃S₂, and 352 mV for NM electrodes under identical conditions (Figure 6b). Considering the instability of reference electrodes at high temperatures, the stability assessment of NiFe-LDH/Ni₃S₂ was conducted using a two-electrode system. Coupled with a Raney Ni cathode, the NiFe-LDH/Ni₃S₂ anode exhibits minimal degradation of cell voltage after a 100-h test at 300 mA cm⁻² (Figure 6c), in stark contrast to the rapid attenuation observed for NiFe-LDH (Figure S19). This underscores that the NiFe-LDH/Ni₃S₂ heterostructure significantly enhances operational stability under harsh industrial conditions. Aiming at industrial applications, the scale-up of electrode synthesis was also verified by facilely preparing a large electrode with an area over 100 cm² in the laboratory, which exhibits relatively identical

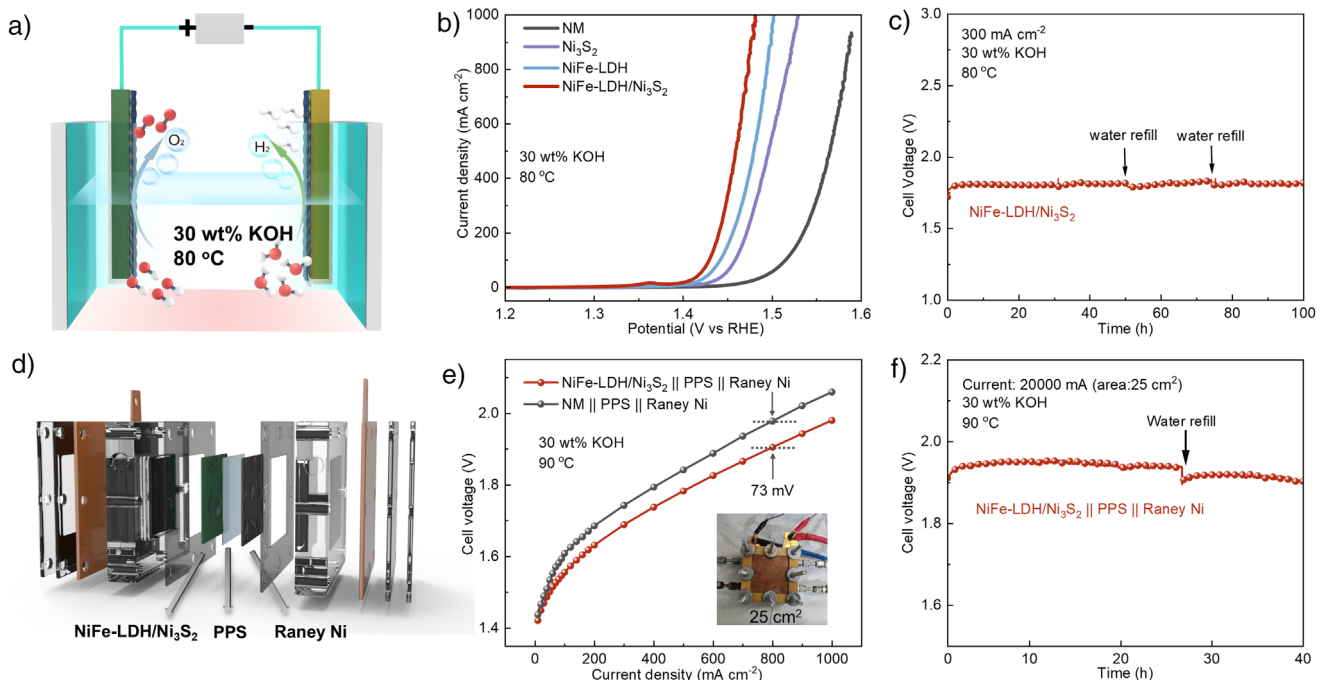


Figure 6. Electrochemical measurements under industrial conditions (30 wt% KOH, 80–90°C). (a) Schematic of water splitting in 30 wt% KOH and at 80 °C. b) Polarization curves obtained in a three-electrode configuration. c) CP test in a two-electrode electrolyzer with NiFe-LDH/Ni₃S₂ anode and Raney Ni cathode at 80 °C. d) Schematic of a homemade alkaline water electrolyzer. e) Polarization curves and f) CP test in the homemade alkaline water electrolyzer at 90 °C.

morphology and almost the same OER performance for four randomly selected regions (Figure S20). The electrocatalytic performance was further evaluated in a homemade alkaline electrolyzer ($5 \times 5 \text{ cm}^2$), utilizing polyphenylene sulfide (PPS) separator as the diaphragm, NiFe-LDH/Ni₃S₂ as the anode, and Raney Ni as the cathode, respectively (Figure 6d). The NiFe-LDH/Ni₃S₂ || PPS || Raney Ni electrolyzer achieves a large current density of 800 mA cm^{-2} at a cell voltage of 1.908 V, superior to 1.981 V required by the NM || PPS || Raney Ni electrolyzer (Figure 6e). Moreover, the NiFe-LDH/Ni₃S₂ || PPS || Raney Ni electrolyzer sustains its performance after 40 h of continuous operation at 800 mA cm^{-2} (Figure 6f), with the NiFe-LDH structure remaining well-organized (Figure S21), confirming its exceptional operational stability in industrial alkaline electrolyzers.

Conclusion

In conclusion, a freestanding NiFe-LDH/Ni₃S₂ heterostructure was successfully synthesized on NM using a straightforward and scalable corrosion-electrodeposition process for application in industrially relevant AWE. The BEF driven by the work function difference and the resulting Fe/Ni–S interfacial bond accelerates the charge redistribution at the interface, thus enhancing OH[−] adsorption, promoting *OH deprotonation, and mitigating Fe leaching at high current densities. Notably, the resultant NiFe-LDH/Ni₃S₂ heterostructure demonstrates remarkable OER activity and stability, featuring ultra-low overpotentials of merely 202 mV

at 10 mA cm^{-2} and 290 mV at 800 mA cm^{-2} in 1.0 M KOH at 25°C , as well as excellent steady-state stability and high resistance to reverse current under fluctuating conditions. Moreover, the electrode performance has been validated in AWE with harsh operation conditions (30 wt% KOH, 90 °C), achieving a current density of 800 mA cm^{-2} with only 1.908 V. This study offers profound insights into the design principles of industrial OER electrodes and illuminates potential avenues for future technological advancements.

Supporting Information

The data that support the findings of this study are available in the Supporting Information of this article.

Acknowledgements

The authors appreciate the support from the National Key Research and Development Program of China (No. 2024YFE0211400), the National Natural Science Foundation of China (No. 22478221), Tsinghua-Jiangyin Innovation Special Fund (TJISF, No. 2024JYTH09), Huaneng Group science and technology research project (No. HNKJ23-H71), Ordos Laboratory, the National Natural Science Foundation of China (No. 52488201, No. 52276212), the National Key Research and Development Program of China (No. 2022YFB3803600), the Natural Science Foundation of Jiangsu Province (No. BK20231211), the Suzhou Science and Technology Program (No. SYG202101), the Key Research

and Development Program in Shaanxi Province of China (No. 2023-YBGF-300), and the China Fundamental Research Funds for the Central Universities.

Conflict of Interests

The authors declare no conflict of interest.

Data Availability Statement

The data that support the findings of this study are available in the supplementary material of this article.

Keywords: Alkaline water electrolysis • Built-in electric field • Freestanding electrodes • Oxygen evolution reaction

- [1] K. Ham, S. Bae, J. Lee, *J. Energy Chem.* **2024**, *95*, 554–576.
- [2] Y. Luo, Z. Zhang, M. Chhowalla, B. Liu, *Adv. Mater.* **2022**, *34*, 2108133.
- [3] C. Tang, Q. Zhang, *Engineering* **2023**, *29*, 22–26.
- [4] L. Du, H. Xiong, H. Lu, L.-M. Yang, R.-Z. Liao, B. Y. Xia, B. You, *Exploration* **2022**, *2*, 20220024.
- [5] N. Wang, S. Song, W. Wu, Z. Deng, C. Tang, *Adv. Energy Mater.* **2024**, *14*, 2303451.
- [6] M. Chatenet, B. G. Pollet, D. R. Dekel, F. Dionigi, J. Deseure, P. Millet, R. D. Braatz, M. Z. Bazant, M. Eikerling, I. Staffell, P. Balcombe, Y. Shao-Horn, H. Schäfer, *Chem. Soc. Rev.* **2022**, *51*, 4583–4762.
- [7] Q. Wen, K. Yang, D. Huang, G. Cheng, X. Ai, Y. Liu, J. Fang, H. Li, L. Yu, T. Zhai, *Adv. Energy Mater.* **2021**, *11*, 2102353.
- [8] W. He, X. Li, C. Tang, S. Zhou, X. Lu, W. Li, X. Li, X. Zeng, P. Dong, Y. Zhang, Q. Zhang, *ACS Nano* **2023**, *17*, 22227–22239.
- [9] S. Yu, X. Yu, H. Yang, F. Li, S. Li, Y. S. Kang, J. Y. Zheng, *J. Energy Chem.* **2024**, *99*, 23–49.
- [10] W. Xu, T. Ma, H. Chen, D. Pan, Z. Wang, S. Zhang, P. Zhang, S. Bao, Q. Yang, L. Zhou, Z. Tian, S. Dai, Z. Lu, *Adv. Fuct. Mater.* **2023**, *33*, 2302263.
- [11] Z. Zhao, J. Sun, X. Li, S. Qin, C. Li, Z. Zhang, Z. Li, X. Meng, *Nat. Commun.* **2024**, *15*, 7475.
- [12] B. Wang, J. Li, D. Li, J. Xu, S. Liu, Q. Jiang, Y. Zhang, Z. Duan, F. Zhang, *Adv. Mater.* **2024**, *36*, 2305437.
- [13] D. Li, R. Xiang, F. Yu, J. Zeng, Y. Zhang, W. Zhou, L. Liao, Y. Zhang, D. Tang, H. Zhou, *Adv. Mater.* **2024**, *36*, e2305685.
- [14] J. Yu, K. Hu, Z. Zhang, L. Luo, Y. Liu, D. Zhou, F. Wang, Y. Kuang, H. Xu, H. Li, H. Duan, X. Sun, *Energy Environ. Sci.* **2023**, *16*, 2068–2079.
- [15] W. Liu, X. Ding, J. Cheng, J. Jing, T. Li, X. Huang, P. Xie, X. Lin, H. Ding, Y. Kuang, D. Zhou, X. Sun, *Angew. Chem. Int. Ed.* **2024**, *63*, e202406082.
- [16] Z. Li, G. Lin, L. Wang, H. Lee, J. Du, T. Tang, G. Ding, R. Ren, W. Li, X. Cao, S. Ding, W. Ye, W. Yang, L. Sun, *Nat. Catal.* **2024**, *7*, 944.
- [17] H. Li, Y. Lin, J. Duan, Q. Wen, Y. Liu, T. Zhai, *Chem. Soc. Rev.* **2024**, *53*, 10709–10740.
- [18] X. Wei, S. Sharma, A. Waeber, D. Wen, S. N. Sampathkumar, M. Margni, F. Maréchal, J. Vanherle, *Joule* **2024**, *8*, 3347–3372.
- [19] Z. Xu, Z.-S. Wu, *eScience* **2024**, 100334.
- [20] T. Wu, E. Song, S. Zhang, M. Luo, C. Zhao, W. Zhao, J. Liu, F. Huang, *Adv. Mater.* **2022**, *34*, 2108505.
- [21] X. Jiang, V. Kyriakou, C. Song, X. Wang, S. Costil, C. Deng, T. Liu, T. Jiang, H. Liao, *J. Energy Chem.* **2024**, *93*, 511–518.
- [22] L. Deng, L. Jin, L. Yang, C. Feng, A. Tao, X. Jia, Z. Geng, C. Zhang, X. Cui, J. Shi, *eScience* **2024**, 100353.
- [23] J. Khan, H. Liu, T. Zhang, X. Kang, Z. Zhang, Y. Dong, S. Li, J. Liu, Q. Yu, B. Liu, *Energy Environ. Sci.* **2024**, *17*, 9435–9442.
- [24] N. Todoroki, K. Nagasawa, H. Enjoji, S. Mitsushima, *ACS Appl. Mater. Interfaces* **2023**, *15*, 24399–24407.
- [25] Y. F. Song, Z. Y. Zhang, H. Tian, L. Bian, Y. Bai, Z. L. Wang, *Chemistry* **2023**, *29*, e202301124.
- [26] M. Yu, J. Zheng, M. Guo, *J. Energy Chem.* **2022**, *70*, 472–479.
- [27] X. Kong, P. Hao, H. Duan, *Exploration* **2021**, *1*, 20210052.
- [28] X. Yang, Q.-Q. Chen, C.-J. Wang, C.-C. Hou, Y. Chen, *J. Energy Chem.* **2019**, *35*, 197–203.
- [29] Z. Wang, W. A. Goddard, III, H. Xiao, *Nat. Commun.* **2023**, *14*, 4228.
- [30] J. Cheng, D. Wang, *Chin. J. Catal.* **2022**, *43*, 1380–1398.
- [31] S. Sebbahi, A. Assila, A. Alaoui Belghiti, S. Laasri, S. Kaya, E. K. Hlil, S. Rachidi, A. Hajjaji, *Int. J. Hydrogen Energ.* **2024**, *82*, 583–599.
- [32] C. Feng, X. She, Y. Xiao, Y. Li, *Angew. Chem. Int. Ed.* **2023**, *62*, e202218738.
- [33] X. Lin, Z. Wang, S. Cao, Y. Hu, S. Liu, X. Chen, H. Chen, X. Zhang, S. Wei, H. Xu, Z. Cheng, Q. Hou, D. Sun, X. Lu, *Nat. Commun.* **2023**, *14*, 6714.
- [34] X. Liu, R. Guo, M. Guo, K. Ni, M. Huang, J. Meng, X. Xie, D. Zhao, L. Mai, C. Niu, *Adv. Mater.* **2024**, *36*, 2313931.
- [35] X. Wang, X. Zong, B. Liu, G. Long, A. Wang, Z. Xu, R. Song, W. Ma, H. Wang, C. Li, *Small* **2022**, *18*, e2105544.
- [36] N. Zhang, Y. Hu, L. An, Q. Li, J. Yin, J. Li, R. Yang, M. Lu, S. Zhang, P. Xi, C. H. Yan, *Angew. Chem. Int. Ed.* **2022**, *61*, e202207217.
- [37] K. He, T. Tadesse Tsega, X. Liu, J. Zai, X. H. Li, X. Liu, W. Li, N. Ali, X. Qian, *Angew. Chem. Int. Ed.* **2019**, *58*, 11903–11909.
- [38] X. Teng, D. Si, L. Chen, J. Shi, *eScience* **2024**, *4*, 100272.
- [39] J. Liu, X. Yang, F. Si, B. Zhao, X. Xi, L. Wang, J. Zhang, X.-Z. Fu, J.-L. Luo, *Nano Energy* **2022**, *103*, 107753.
- [40] W. Zhang, L. Yang, Z. Li, G. Nie, X. Cao, Z. Fang, X. Wang, S. Ramakrishna, Y. Long, L. Jiao, *Angew. Chem. Int. Ed.* **2024**, *63*, e202400888.
- [41] S. Zhao, Y. Wang, Y. Hao, L. Yin, C. H. Kuo, H. Y. Chen, L. Li, S. Peng, *Adv. Mater.* **2023**, e2308925.
- [42] Q. Jiang, S. Wang, C. Zhang, Z. Sheng, H. Zhang, R. Feng, Y. Ni, X. Tang, Y. Gu, X. Zhou, S. Lee, D. Zhang, F. Song, *Nat. Commun.* **2023**, *14*, 6826.
- [43] M. Klingenhof, H. Trzesniowski, S. Koch, J. Zhu, Z. Zeng, L. Metzler, A. Klinger, M. Elshamy, F. Lehmann, P. W. Buchheister, A. Weisser, G. Schmid, S. Vierrath, F. Dionigi, P. Strasser, *Nat. Catal.* **2024**, *7*, 1213–1222.
- [44] A. Abdel Haleem, K. Nagasawa, Y. Kuroda, Y. Nishiki, A. Zaenal, S. Mitsushima, *Electrochemistry* **2021**, *89*, 186–191.
- [45] K. Wang, R. Mao, R. Liu, J. Zhang, H. Zhao, W. Ran, X. Zhao, *Nat. Water* **2023**, *1*, 1068–1078.
- [46] X. Bai, M. Zhang, Y. Shen, X. Liang, W. Jiao, R. He, Y. Zou, H. Chen, X. Zou, *Adv. Fuct. Mater.* **2024**, *34*, 2400979.
- [47] X. Liu, R. Guo, K. Ni, F. Xia, C. Niu, B. Wen, J. Meng, P. Wu, J. Wu, X. Wu, L. Mai, *Adv. Mater.* **2020**, *32*, e2001136.
- [48] X.-M. Lin, Y.-L. Sun, Y.-X. Chen, S.-X. Li, J.-F. Li, *eScience* **2024**, 100352.
- [49] X. Shen, H. Li, Y. Zhang, T. Ma, Q. Li, Q. Jiao, Y. Zhao, H. Li, C. Feng, *Appl. Catal. B Environ. Energy* **2022**, *319*, 121917.
- [50] S. Sidra, V. H. Hoa, D. H. Kim, *J. Energy Chem.* **2025**, *103*, 264–273.

Manuscript received: March 02, 2025

Revised manuscript received: March 22, 2025

Accepted manuscript online: March 25, 2025

Version of record online: April 07, 2025